Experimental Verification of Kinematics and Kinetics in a Biomimetic Bipedal Robot

Alexander G. Steele
Agile and Adaptive Robotics Laboratory,
Department of Mechanical and Materials Engineering,
Portland State University,
Portland, OR 97201
e-mail: agsteele@uh.edu

Apploinaire Etoundi
Senior Lecturer Bristol Robotics Laboratory,
Department of Engineering Design and Mathematics,
University of the West of England,
Bristol BS16 1QY, UK
e-mail: Appolinaire.Etoundi@uwe.ac.uk

Alexander J. Hunt[1]
Assistant Professor
Agile and Adaptive Robotics Laboratory,
Department of Mechanical and Materials Engineering,
Portland State University,
Portland, OR 97201
e-mail: ajh26@pdx.edu

This article presents experimental test results for joints used in a biomimetic bipedal robot. In this work, magnetic resonance imaging (MRI) and computed tomography (CT) scans are utilized to inform the design of joints of similar size and function to the biological counterparts. Three lower body joints, to be actuated by artificial muscles, were designed and constructed. Then the range of motion and passive stiffness were tested. The knee joint consists of a four-bar mechanism that provides increased extensor moment arm as the joint becomes more flexed, a "screw home" locking mechanism analog, and large contact surfaces for force distribution. The hip, ankle, and foot are hybrid hard-soft joints, consisting of a ball and socket held together with an outer, inflatable sleeve made from a braided pneumatic actuator (BPA) material. These joints provide a novel way for real-time stiffness adjustments and energy storage during the gait cycle. Results show that the physical knee prototype matches the previous simulation of joint movement (Steele, A., Hunt, A., and Etoundi, A., 2018, "Biomimetic Knee Design to Improve Joint Torque and Life for Bipedal Robotics," Bristol, UK.). A linear relationship exists between the increase in angle and the force required to bend the hybrid joints. First, this article documents a process that others may use to develop their own joints. Second, the range of motion and passive forces in the hybrid hard-soft joints is characterized, which will enable improved control of the joints and inform other researchers to whether a hybrid joint design is appropriate for their applications. This process has several applications in prosthetic designs and robotics.
[DOI: 10.1115/1.4054441]

Keywords: bio-inspired design, compliant mechanisms, legged robots, mechanism synthesis, mobile robots, robot design

1 Introduction

Human balance and locomotion control is highly complex and not well understood. Circuits within the spinal cord generate stepping motions and distribute control to the various muscles in the body—sensory feedback helps coordinate those motions and maintain balance, and high-level control directs motions. Knowledge about these systems is most frequently gained through behavioral experiments, either of humans performing specific actions or through generalization of neural circuit experiments performed on other mammals such as mice and cats. This knowledge is then formalized into neural and control models, which must then be tested in either simulation or on robotic systems to determine their validity [2].

For testing, simulations and robots play complimentary roles. Changes to both a mathematical model and its control system can be implemented quickly in simulation. However, object interaction and ground contact are difficult to simulate with enough accuracy. Therefore, bio-inspired robots help us study how these interactions, i.e., the basis of locomotion, influence neural control [3,4]. Several humanoid bio-robots have demonstrated how the unique musculature and bone arrangement of the human body provides natural dynamics that may simplify control. For example, Asano et al. used human proportions and muscle arrangements to build a robot that had similar body proportions and abilities of the average human; by focusing on mimicking the human foot, the robot was able to use its toes for stabilization, similar to humans [5]. Other examples of insights gained from biomimetic robots include designing robots to perform everyday tasks like getting out of a vehicle [6]. Shin et al. tested a humanoid robot to gain better understanding of how the muscles around the pelvis contribute to the stability and adaptive capabilities of bipedal locomotion [7]. Asano et al. demonstrated how the human knee improves locomotion and reduces power consumption [8].

These robots have been very successful at demonstrating some control strategies; however, there are many simplifications in their designs that limit the types of control questions they might answer. For example, it is difficult to capture both the ball-and-socket joint of the hip [9] and the unique changing center of rotation of the knee [10] without advanced manufacturing capabilities. Robotic joints that are not directly driven by a motor are also typically designed to be as frictionless as possible so as not to interfere with the controller, yet most human joints have passive stiffness and damping associated with them. It is our hypothesis that a more accurate and complete robotic model of human kinematics and kinetics is required to fully understand the human neural control system, which evolved to control a human muscular system, not motors.

This article presents the development of the "bones" of a new robotic system that more closely matches the kinematics and passive dynamics of the human skeletal system when compared to other humanoid robots (Fig. 1). Novel advances of this robot include the use of medical scans to produce a robotic model, the inclusion of joint stiffness in the synovial joints, and detailing of novel knee joint. To match the kinematics, computed tomography (CT) and magnetic resonance imaging (MRI) scans were used to produce 3D models that interact using similar sliding and rolling motions as in the human skeleton. The 3D models are then printed using a multi-material printer that is capable of utilizing continuous carbon fiber, producing robot parts that capture the anatomical accuracy of the body and can stand up to the stresses of robotics research. In addition, attempts were made to capture joint stiffness and range of motion (ROM) associated with synovial joints at the hip and ankle. This article details the design process then determines the kinematic and kinetic properties of the 3D-printed robotic skeletal system.

2 Materials and Methods

2.1 Overview. The design process for each joint in the robot is as follows: first, medical CT and MRI scans of healthy subjects that

[1]Corresponding author.

Contributed by the Mechanisms and Robotics Committee of ASME for publication in the Journal of Mechanisms and Robotics. Manuscript received September 22, 2021; final manuscript received April 18, 2022; published online June 6, 2022. Assoc. Editor: Chin-Hsing Kuo.

Fig. 1 The fully assembled bipedal robot seen anteriorly without inflation of the synovial joints

match the desired robot size were identified and converted to solid surface .stl files for each "bone" in the joint. Then, for each bone, the resultant surfaces were simplified and smoothed to ensure proper mating between the two surfaces. Next, the bones were combined in a SOLIDWORKS® assembly, and motion between them was simulated. Additional mechanical features were added to the bones to limit or improve ROM and stability. After simulations, the models were 3D printed for physical testing and assembly into the complete robot.

2.2 Medical Scans to 3D Model Process. CT scans and MRI scans were used to develop the joint models. CT scans use multiple X-rays taken at different angles to produce cross-sectional images. These scans are exceptional for looking at bones, but do not provide a clear picture of soft tissues without the aid of contrast. MRI scans use strong magnetic fields, radio waves, and field gradients to generate cross-sectional images. MRI scans are excellent at detecting slight differences in tissue and are better for visualizing tendons and ligaments, but the visible soft tissues make it difficult to localize bone. Therefore, both scan types are necessary to develop a clear understanding of the bone structures and kinematics.

Medical scans in the form of Digital Imaging and Communications in Medicine (DICOM) files were obtained from two different sources. The first by using 3D SLICER software, which searches an open-source repository called Medical Connections Activation [11]. The majority of the scans were obtained from the second source, an open-source biomedical 3D printing community called embodi3d where anonymized raw medical scans were downloaded [12]. At the time of the Medical Connections Activation database query, there was no complete set of joints in both scan types from a single healthy subject. Therefore, several different scans of each type were obtained for each joint from healthy male subjects and ranked using the following criteria: (1) preference was given to files of persons that fell into the same age, height, and weight range to minimize the differences between scans, and (2) the slice thickness needed to be as small as possible to maximize the fidelity of the 3D model [13].

The process of turning medical scans into a 3D model using 3D SLICER is outlined in Fig. 2 and described next. 3D SLICER was chosen because it is capable of processing both CT and MRI scans. It parses the different scans and acquires measurements of tendons directly from the joints themselves.

First, the chosen medical scans in DICOM format were imported into the 3D SLICER software (Fig. 2(*a*)). The software automatically assembles the scans into a model by organizing the scans. Next, the threshold tool was used to automatically select and label sections of each layer of the scan within upper lower contrast bounds (Fig. 2(*b*)). The software cannot ensure its selections are contiguous and often selects unwanted tissues outside the bone. Corrections to the model were made through manual segment verification (Fig. 2(*c*)). This step ensures the correct areas of the scan are selected; however, it requires manual fixes to any discontinuities or erroneous selections. After verifying the proper areas are selected, the selections were converted in the software into a 3D model (Fig. 2(*d*)). Each layer is made 3D by extruding the image to the thickness of the MRI or CT scan slice thickness, in this case 1 mm.

Next, the model was smoothed. Figure 3 shows an overview of how the model is finished. The model was exported from 3D Slicer and into MESH MIXER (Fig. 3(*e*)) [14]. This software smooths the scans by determining and maintaining tangent continuity (Fig. 3(*f*)). Tangent continuity occurs when two curves share a common endpoint and are tangent to one another at that point. A high-fidelity model that limits deformation from this process is created by maintaining tangent continuity preferentially over

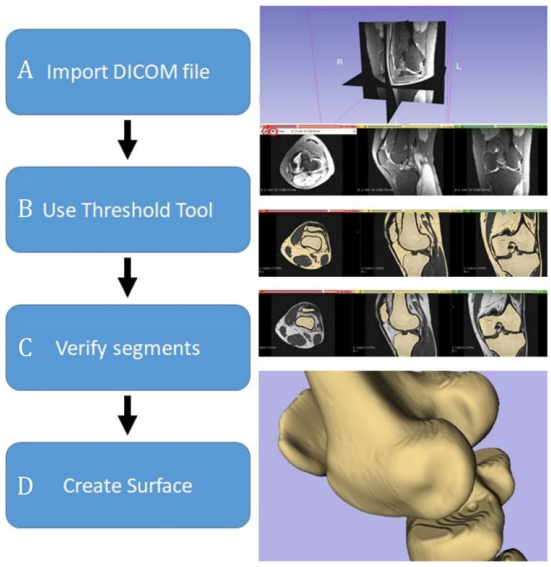

Fig. 2 Overview of creating a solid model using medical scans via the 3D SLICER software. After importing the model into 3D SLICER, the threshold tool is used to select bones automatically. The automatic selection is then manually corrected and then extruded.

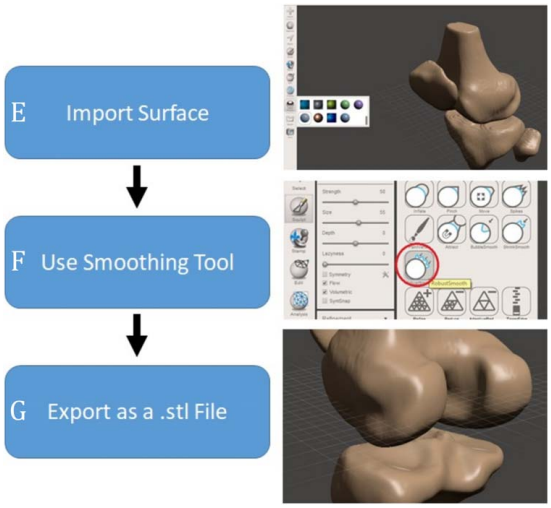

Fig. 3 The 3D SLICER model is smoothed by using the tangent continuity tool in MESH MIXER and exported for use in SOLIDWORKS®

other smoothing operations where "flattening" or oversmoothing effects could occur. Finally, the file was exported as a .stl file (Fig. 3(*g*)).

2.3 Leg Components

2.3.1 Pelvis. The pelvis consists of the sacrum, coccyx, and hip bones. In the human skeletal system, these bones are connected by several thick ligaments [15]. These flexible connections help the hip absorb impact loading when walking and running, which leads to a more energy efficient gait [16]. To take advantage of these same properties, our design includes the three separate bones, with the sections connected using braided pneumatic actuators (BPAs) (Festo DMSP-20) [17]. After the initial 3D model was developed based on the process described earlier, a flange was added to the bones to enable connection of 20 mm BPAs, and internal cavities were added to allow inflation of all three of the connection points through one valve port. When inflated, these actuators provide some compliance, but remain relatively stiff. The stiffness of this can be adjusted by changing the internal pressure, although this is not explored in this article.

2.3.2 Hip. The hip joint is a ball-and-socket joint where the femoral head of the femur is the ball, and the acetabulum of the pelvis creates a cup-like depression in which the femoral head fits [18]. To simplify design and construction, the ball-and-socket was modeled as a perfect sphere with a radius of 18.41 mm, slightly smaller than the average adult male 24.53 ± 1.74 mm [19]. The ROM of the hip varies with age and gender. The average ROM for the adult male in the United States can be seen in Table 1 [20,21].

The hip joint is a synovial joint. A synovial joint is characterized as a joint that is surrounded by a joint capsule—a dense and fibrous structure that is like a tendon—which forms a sleeve around the joint. Stiffness in this structure is thought to be the primary way the body reduces the need to activate muscles to help remain upright [22,23]. To replicate this stiffness, the ball-and-socket is surrounded with a BPA and the system is pressurized. Results for different pressures and the effect on joint stiffness are presented and discussed later. The socket of the designed hip was created asymmetrically so that the BPA could be clamped tightly enough to create a reliable seal.

Table 1 Maximum range of motion for the hip joint in a healthy adult male given in deg

Flexion	120 deg
Extension	12 deg
Adduction	51 deg
Abduction	61 deg
Internal rotation	32 deg
External rotation	36 deg

2.3.3 Femur. The femur has several different geometric parameters that affect the strength of the bone [24,25]. One consideration for the femur is the quadriceps angle (q-angle). The q-angle is the angle formed by the femur and the hip relative to the ground as shown in Fig. 4(*a*). It is defined as the angle between a line formed by the resultant force of the quadriceps, made by connecting a point between the anterior superior iliac spine to the midpoint of the patella and a second line from the central patella to the tibial tubercle [26]. Forces applied via the quadriceps muscle to the patella are reduced as the q-angle is increased; however, as this angle increases, the risk factor for patellar dislocation and femur fracture increases [27]. While q-angle differs between subjects and age, for healthy men between 18 and 35 years, the average q-angle is 13.5 ± 4.5 deg. For females, the q-angle is larger: 18.1 ± 4.5 deg is considered the healthy range for subjects between 18

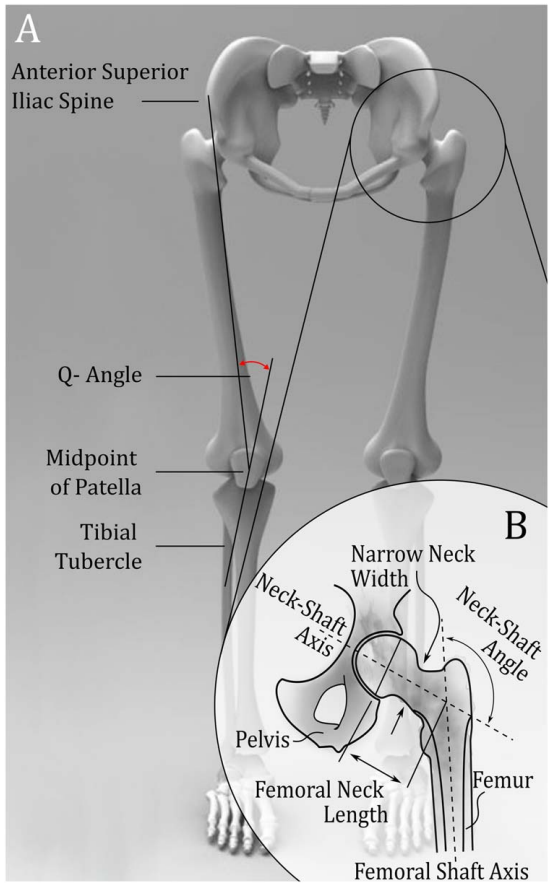

Fig. 4 Geometric considerations for designing the hip joint and head of the femur: (*a*) The quadriceps angle (q-angle) is the angle the quadriceps muscle attaches to the patella and is measured using the anterior superior iliac spine, midpoint of the patella, and the tibial tubercle and (*b*) Narrow neck width is measured at the narrow point of the femoral neck. The femoral neck length is determined by the center of the femoral head to the intersection of the neck-shaft axis and the femoral shaft axis. Finally, the neck-shaft angle is the angle between the neck-shaft axis and the femoral shaft axis. These variables are important for design consideration because in humans, they are markers for fracture.

and 35 years [26,28]. The q-angle chosen for this robot is 15.75 deg, which is within the average range for the male q-angle.

Other geometric considerations are shown in Fig. 4(*b*). They include the femoral neck length, the narrow neck width, and the neck-shaft angle. The neck of the femur is especially at risk of fracture due to the cyclical loading conditions during walking. To reduce the risk of fracture, one may assume that a large neck width would be preferable. However, despite conventional wisdom, there is evidence that a larger neck width could increase risk of fracture as there is an interplay between the angle of the shaft, shaft width, and neck length [29]. The joint geometry in our design comes from the median values of an adult male, not directly from the medical scans [30]. The values used are as follows: femoral neck length = 26 mm, narrow neck width = 28 mm, and neck-shaft angle = 130 deg.

2.3.4 Knee. The human knee is one of the most complex joints in the human body, containing 6 degrees-of-freedom (DOF) [31,32]. The average maximum extension of the knee in adult males is 2.5 ± 2.9 deg, while the average maximum flexion in the adult male knee is 137.5 ± 9.6 deg [33]. This gives the knee a total ROM—for both flexion and extension—140 deg. The knee has been modeled several different ways, using kinematic data, in vivo studies, and even ex vivo studies [34–38]. Our method uses in vivo data to create a 3D model to extract the underlying geometry and kinematics.

The design only models the prominent DOFs involved in locomotion: flexion/extension and axial rotation. In addition, the joint rotations are decoupled such that flexion/extension occurs proximal to axial rotation. A four-bar mechanism is used to capture the changing center of rotation that occurs during flexion/extension. This changing center of rotation changes the moment arms of muscles actuating about the knee joint, therefore affecting the total torque output. In addition, the design ensures continued contact between the surfaces of the femur and tibia, bearing the load of the robot and reducing forces applied to the pins on the mechanism. Figure 5 shows the knee fully assembled as it travels through the ROM for the joint. Additional details regarding joint design and moment arm can be found in our previously published papers [1,39].

Unlike the hip and ankle, the robot knee is a rigid joint. The force required to move the joint through its ROM is minimal and is only dependent on the friction between the linkages. However, this joint does have a locking mechanism when standing [1]. This is analogous to the "screw home" mechanism found in the human knee [31].

When fully extended the human knee rotates externally by roughly 20 deg. This locks the knee so that no muscle strength is required to remain in this position. A similar energy saving mechanism was designed into our knee [1]. Figure 6(*a*) is a cut away of the knee in the fully extended position; the links demonstrate the 4-bar mechanism when link 1 is in the forward position.

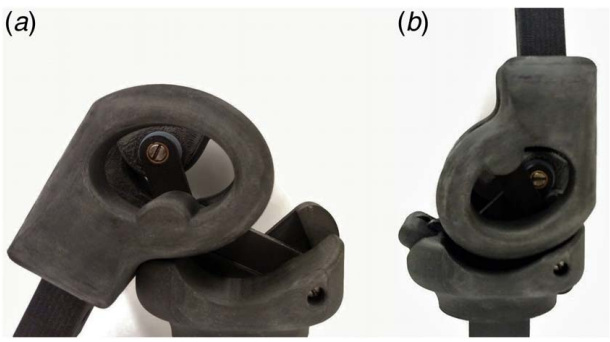

Fig. 5 Sagittal view of the assembled knee joint during (*a*) full flexion and at and (*b*) full extension

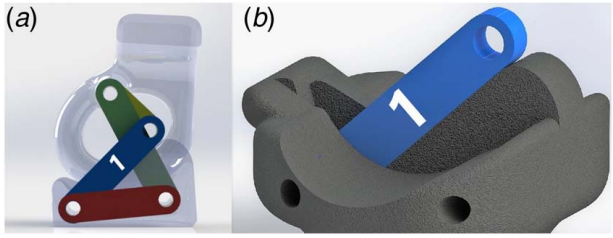

Fig. 6 (*a*) Sagittal and cutaway view of the knee showing the 4-bar linkage. Link 1 is in the forward position when the knee is fully extended. However, it cannot move further forward because of and (*b*) the mechanical stop created to prevent further rotation of the linkage.

Figure 6(*b*) is an exploded view showing link 1 and the mechanical stop that keeps the knee from rotating further forward. The amount of force needed to unlock the joint is a function of the amount of weight that is loaded to the knee; therefore, the heavier the load, the higher the perpendicular force that is required to unlock it.

2.3.5 Ankle. In humans, the ankle is categorized as a 1DOF Mortise and Tenon joint called the talocrural joint, which provides dorsiflexion/plantarflexion (Fig. 7). However, a second 1DOF joint, directly under the talocrural joint—called the subtalar joint—provides inversion and eversion motion to the foot [40–42]. Table 2 presents the ROM of the human ankle in the adult male.

The subtalar joint has no bony reinforcement, instead it is held in place by ligaments. Since the subarticular joint has to depend on the ligaments and musculature of the foot to remain in place, it is this subtalar joint that typically causes instability in the ankle joint and is the frequent cause of ankle sprains [40,42]. By eliminating the stacked single degree-of-freedom joints, which make up the ankle, the joint is simplified as a ball-and-socket joint with an asymmetrical configuration, and joined by an artificial muscle that limits axial rotation, similar to the hip joint (Fig. 8(*a*)). This was done because the ROM of a human foot is higher for plantarflexion than dorsiflexion [40]. Although this would theoretically create an additional degree-of-freedom, the artificial muscle does not provide significant rotational capability, limiting rotational movement. This is addressed in more detail in the discussion section.

2.3.6 Foot. The human foot is made up of the lateral, medial, and transverse arches, which act as springs in the foot [43]. The

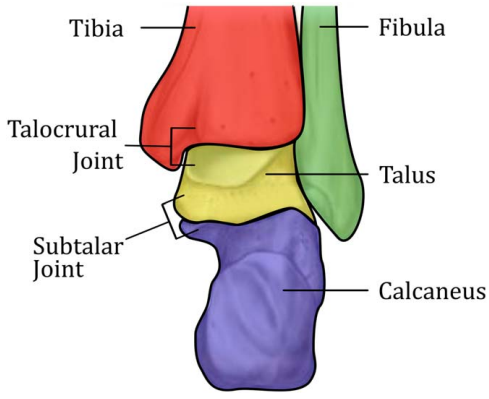

Fig. 7 Posterior view of the ankle joint. The fibula and tibia form the mortise, while the articular surface of the talus creates the tenon. Alone, this is a strong configuration, but only provides 1DOF. The subtalar joint formed by the talus and calcaneus and has only ligaments for support, making it mechanically weaker than the talocrural joint above it.

Table 2 Minimum and maximum range of motion of the ankle joint in the average adult male given in deg

Plantarflexion	59 deg
Dorsiflexion	71 deg
Inversion	42 deg
Eversion	56 deg

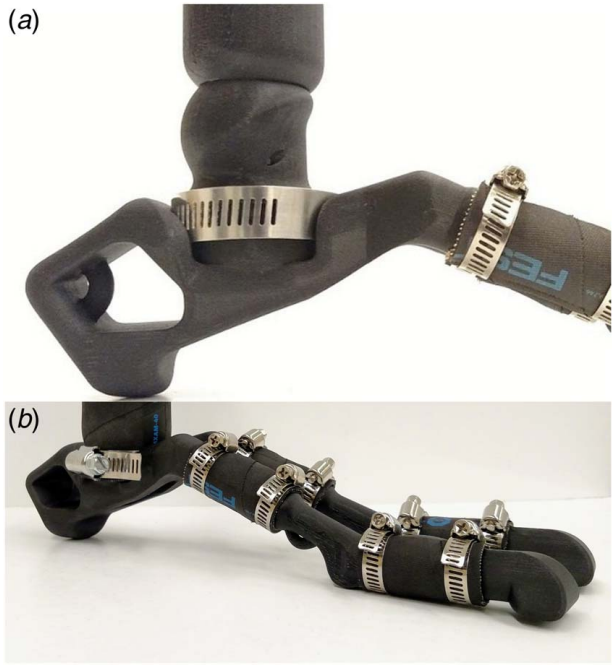

Fig. 8 (*a*) Contacting surfaces of the ankle joint as seen laterally. The asymmetrical contact surface of the foot gives a greater range of motion during plantarflexion and (*b*) Two-toed design simplifies the design without impacting function.

lateral arch uses ligaments and muscle to connect the lateral toes, shown as the dark blue section seen in Fig. 9, to the lateral plantar section of the foot, shown in light blue. The medial arch does the same for the medial side; it connects the medial plantar to the medial toes. The transverse arch is different in that it connects the lateral and medial toes. Arch function changes dynamically during the gait cycle, which is why people who have abnormally high or low arches have trouble with walking [43,44]. Hashimoto et al. showed that a natural gait could be achieved by simplifying the foot to just two halves, a lateral half, (left), and medial half (right) in Fig. 9 [44]. Thus, the foot can be simplified, underactuated, and still achieve a normal human-like gait.

Figure 8(*b*) shows the designed two-toed robotic foot. Each toe has two joints that act as the lateral/medial plantar and the lateral/medial toes. Like the ankle and hip, the joints are a hybrid of soft and hard materials, using a pneumatic muscle as the synovial covering to ball-and-socket contacts within the foot bones. Care was taken to duplicate the function of the lateral, medial, and transverse arches in the design instead of using the flat foot simplification. The transverse arch is achieved by the attachment of a 50.8 mm Festo DMSP-10 to the heel plug inside the designed calcaneus (not shown attached). At the opposite end of the air muscle, a plug is attached to seal and inflate it, along with an attached braded Kevlar cord that acts as the tendon and connects the lateral and medial plantar sections of the foot. The medial attachment point is shown in Fig. 8(*b*) as a half ring just below the medial plantar joint.

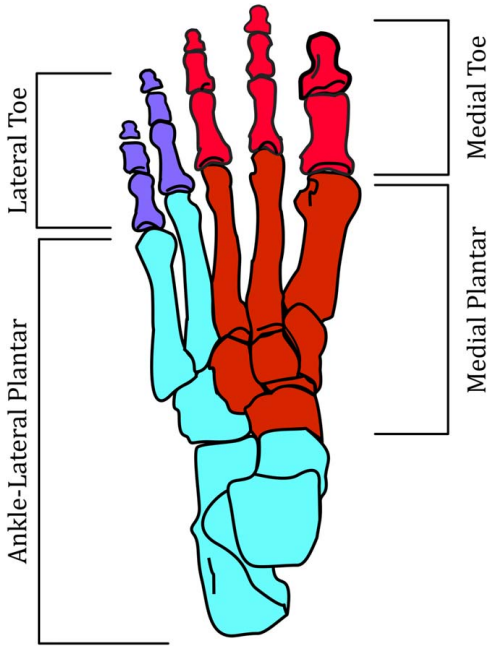

Fig. 9 Transverse plane view of the bones of the left foot. The ankle-lateral plantar and lateral toe act as one unit, while the medial plantar and medial toe act as another unit

A hollow tube runs through the center of each section such that when the ankle is inflated the other sections of the foot inflate as well. This design increases the internal pressure of the ankle during the toe off phase of gait due to the compression of the internally connected BPA that make up the toe joints effectively adjusting joint stiffness during the gait cycle without the need for manual control. The adaptation of ankle stiffness during the gait cycle is similar to how the human body has been shown to work [45,46].

2.4 Construction

2.4.1 3D Printing. Construction was done using a MarkForged 3D printer. This printer has the unique ability to add continuous fiber to the nylon and carbon fiber chop composite base as shown as a cutaway in Fig. 10. These include Kevlar, fiberglass, high temperature-high strength fiberglass, or carbon fiber [47].

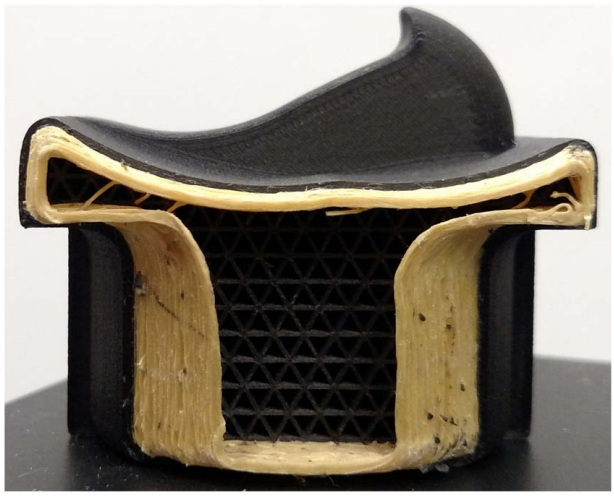

Fig. 10 Side view of a 3D print where the outer nylon/carbon fiber layer has been removed to expose the Kevlar layer underneath

Each material gives the print different properties. For our parts, Kevlar is used to increase the life of components that roll, slide, or require high tensile strength [48]. Parts that include Kevlar are the feet, knees, and hip joints. Carbon fiber is used to add rigidity to a part, along with giving the part a high strength to weight ratio [49]. Parts that include carbon fiber are the hips and the tibial and femur shafts.

2.4.2 Postprocessing. Once printed, each part had support material removed and was sanded. Next, a thin coat of food grade mineral oil was applied, and the part was manually heated using a heat gun. This was done for cosmetic purposes as the sanded part has a dull and uneven looking exterior, and to remove some of the residual stresses from printing [50].

2.5 Joint Testing

2.5.1 Kinematics. Range of motion (ROM) for each of the joints was tested by clamping the proximal body of the joint and applying force to the distal body until a joint limit was reached. Then the force direction was reversed until the other joint limit was reached. The angle at these two extremes was measured using a standard protractor centered at the initial center of rotation. The total ROM is calculated as one extreme minus the other. For the hip and ankle joints, this was repeated nonsequentially over increasing initial joint pressures ranging from 20 psi to 80 psi. Five trials for each joint were collected; the average and standard deviation of the five trials are reported.

2.5.2 Passive Stiffness. Testing the passive properties of the joints was done in a similar manner to the kinematics. However, instead of pushing the joint by hand, a string was attached at a fixed distance from the joint and pulled perpendicular to the bone. A constant force was applied by hand and was measured using a Modern Step brand digital spring scale. The angle of this force was kept constant relative to the initial position of the joint in relation to the pull angle. When the joint settled, the angle was recorded using a protractor. The torque required to move the joint is calculated by:

$$T = F * L * \cos(\theta) \tag{1}$$

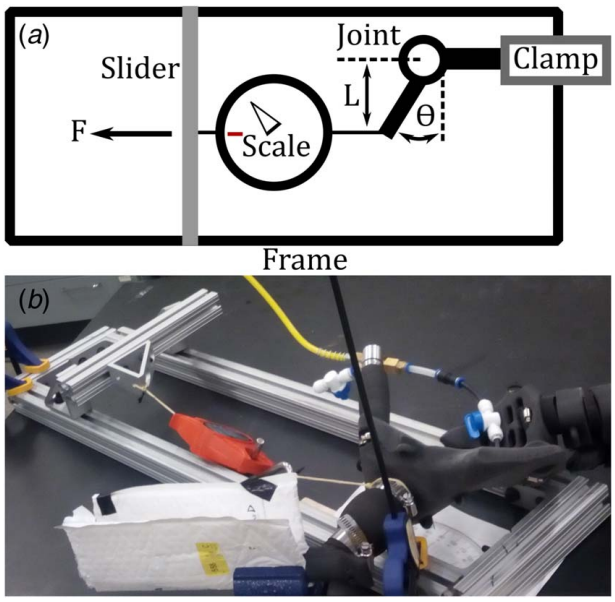

Fig. 11 (*a*) Diagram of testing rig used oriented to match the and (*b*) photo during tests with the constructed rig created to apply a force at a constant angle independent of the angle of the joint

where T is the produced torque, F is the applied force, L is the distance from the applied force to the centroid of the joint, and θ is the change in the angle of the joint. Figure 11 shows (*a*) a diagram of the test rig and (*b*) a photo of the constructed testing rig used during the experiment. Each joint was tested five times, changing the tested joint between each trial. The starting pressure for the tests ranged between 20 and 80 PSI in increments of 20 PSI. The amount of force applied ranged between 5 and 45 N m.

3 Results

3.1 Overall Results. After assembly, and before pressurizing of the joints, the robot skeleton can stand without actuation (Fig. 1). This is due to the stiffness of the hybrid joints and self-locking mechanism at the knee. This ability to stand without actuation could reduce energy consumption of the robot when it is not moving. The robot weighs 10 kg (22 pounds), has a height of 121 cm, a leg length of 91 cm, and a base of support of 31 cm in width and 25 cm in depth.

3.2 Hip Range of Motion. Rotation at the hip is affected by the amount of initial pressure supplied to the joint. Joint limits occur when the angle of the joint causes contact between the joint surfaces, which generates high resistance to additional bending. In addition, increasing the initial pressure also limits the joint's ROM. Figure 12(*a*) shows the ROM for adduction and abduction of the robot joint as depicted on the SOLIDWORKS model with a starting pressure of 20 psi, increasing in 20-psi increments to 60 psi, all measurements are given in deg.

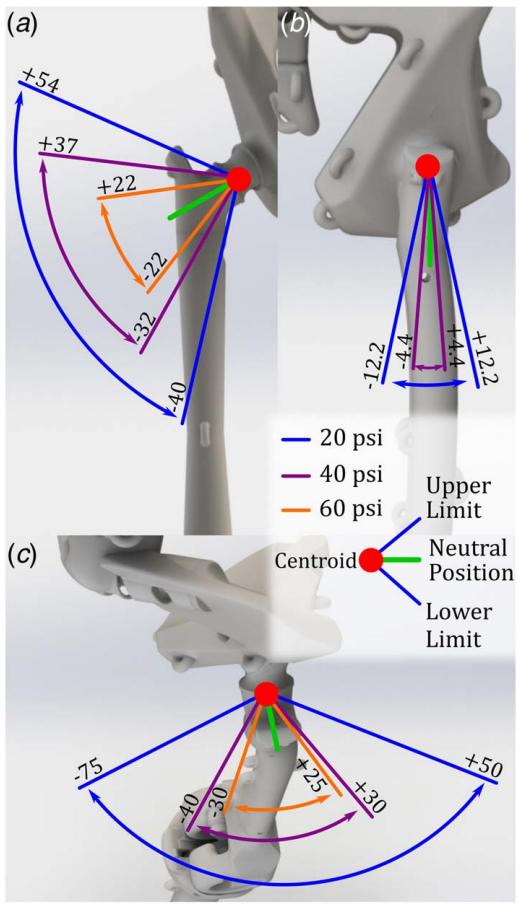

Fig. 12 Range of motion of the designed hip joint during (*a*) abduction/adduction, (*b*) flexion/extension, and (c) internal/external rotation over a range of initial air pressures. All angles are in deg.

The pneumatic air muscles that were used in construction of the robot do not easily twist, so the flexion and extension ROM of the hip are very limited. This limitation will be addressed in future work. Figure 12(*b*) shows the extension and flexion ROM for the hip.

Figure 12(*c*) shows the ROM of the designed hip joint during internal and external rotation with a starting air pressure of 20 psi and a maximum of 60 psi. All measurements are given in deg. As was expected from the design, the amount of rotation is not symmetrical; this is due to the asymmetric flange used to attach the BPA to the joint.

3.3 Knee Range of Motion. The robot knee has a maximum extension of 1 deg and flexion of 150 deg. Figure 13 shows the knee ROM. The total ROM for the knee is 151 deg, which matches the average adult male knee [33].

3.4 Ankle Range of Motion. Like the hip, the ankle ROM is a function of the supplied pressure. Increased pressure causes a smaller ROM. Figure 14(*a*) shows the maximum deg of eversion and inversion for the designed ankle joint at different initial pressures.

The joint was designed asymmetrically, so the differences in the ROM for dorsiflexion and plantarflexion are expected. Figure 14(*b*) shows the ROM, given in deg, utilizing different initial pressures for the designed ankle joint during dorsiflexion and plantarflexion. The maximum ROM for plantarflexion is indeed higher across every initial pressure than the joint can achieve when in dorsiflexion.

3.5 Hip Stiffness. Figure 15 shows the torque required to (*a*) abduct and (*b*) adduct the hip joint at different initial inflation pressures. This internal resistance acts as a restorative force and provides a way for the robot to stand without using energy in powering actuators. These data are also compared with estimates of stiffness on a human hip [51]. The linearized stiffness for the human joint is approximately 0.32 Nm/deg (18.33 Nm/rad) for abduction and 0.84 Nm/deg (48.13 Nm/rad) for adduction. The stiffness of the robot is even closer to linear, but is stiffer than a human. The stiffness at 20 psi (the closest to that of a human) is 1.8 Nm/deg (103.13 Nm/rad) for abduction and 1.5 Nm/deg (85.94 Nm/rad) for adduction.

When testing the flexion/extension of the hip, unintended out of plane bending occurred when attempting to record the data that could not be corrected using our measuring rig; therefore, the measurements were not recorded. This occurred because the stiffness in flexion/extension is much greater than in abduction/adduction and in rotation.

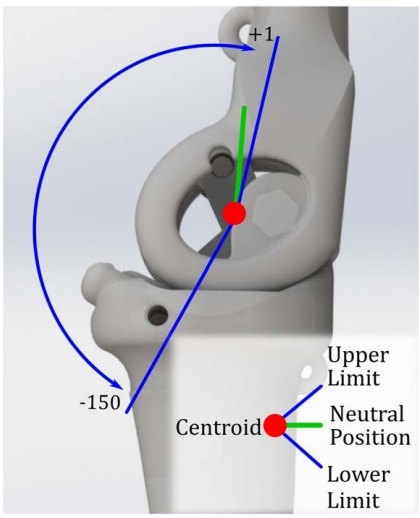

Fig. 13 Designed knee range of motion for full extension and full flexion, the total range of motion is roughly 151 deg. This falls within the typical knee range of motion of 2.5 ± 2.9 deg in extension and 137.5 ± 9.6 deg in flexion [33].

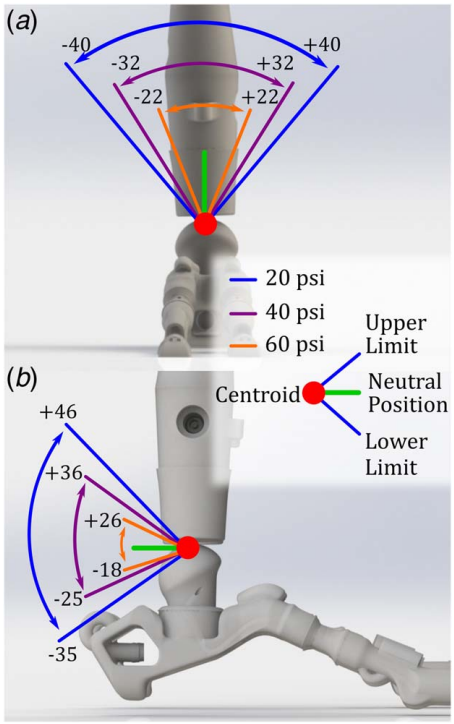

Fig. 14 Range of motion of the designed ankle joint during (*a*) eversion/ inversion and (*b*) plantarflexion/dorsiflexion with different initial pressures. All angles are in deg.

3.6 Ankle Stiffness. Figure 16 shows the torque required to move the ankle joint during (*a*) dorsiflexion and (*b*) during

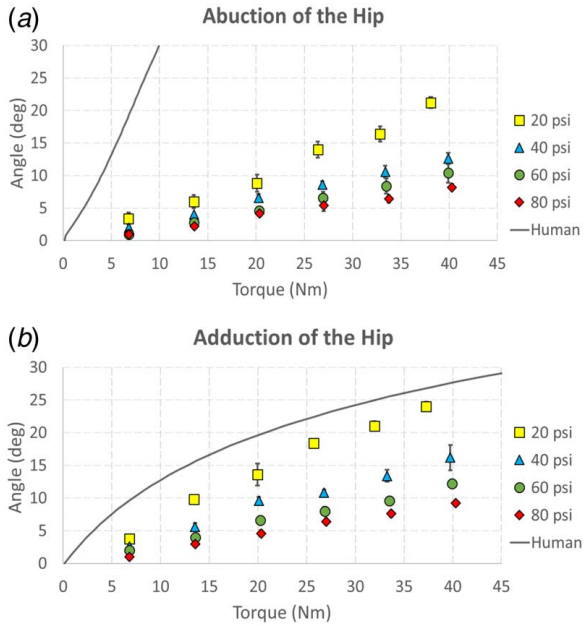

Fig. 15 Average torque required to move the hip joint with different initial pressures for five nonsequential trials of (*a*) abduction and (*b*) adduction; standard deviation from these trials is also shown. Both are plotted with the human model of hip flexion (black line).

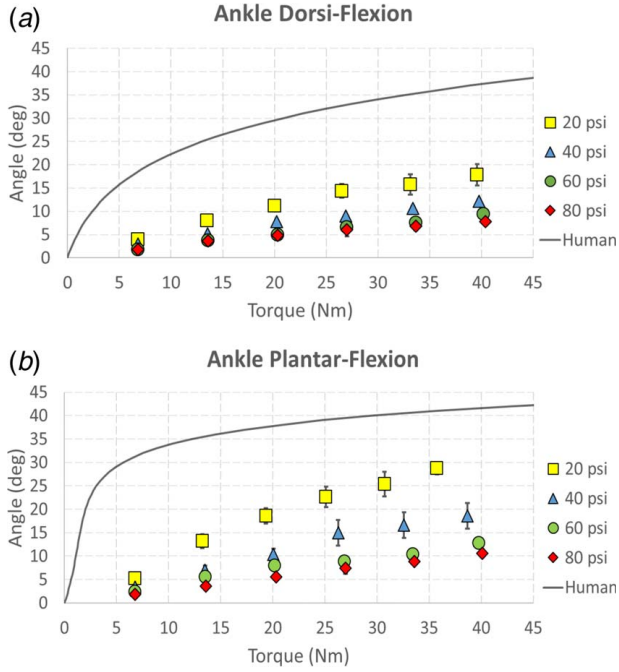

Fig. 16 The average restorative forces for the ankle over five nonsequential trails at different initial pressures ranging from 20 psi to 80 psi for (*a*) dorsiflexion of the ankle and (*b*) plantarflexion of the ankle; standard deviation from these trials is also shown. Both are plotted with the human model for plantarflexion (black line).

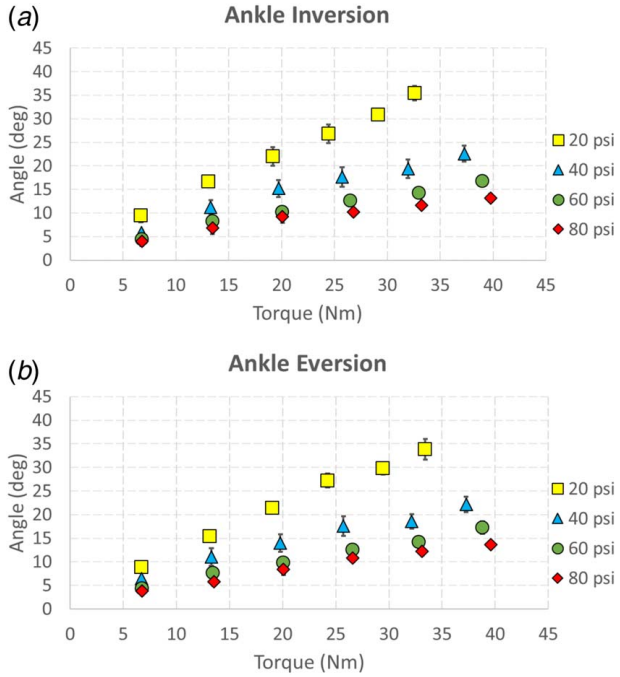

Fig. 17 Average restoring force of the ankle over five nonconsecutive trials for a range of initial pressures ranging from 20 psi to 80 psi for (*a*) ankle inversion and (*b*) eversion. Standard deviation from these trials is also shown.

plantarflexion. Like the human ankle, the designed joint has a torque that changes with the angle of deflection.

The torque required to rotate the ankle in dorsiflexion is higher than during plantarflexion. For a given force at an initial pressure, the ankle rotates more in plantarflexion than in dorsiflexion. This disparity between the two results is likely caused by the asymmetric design of the ankle as shown in Fig. 8. These data are also compared with estimates of stiffness on a human ankle [51]. The linearized stiffness for the human joint is approximately 0.16 Nm/deg (9.17 Nm/rad) for 0–30 deg in plantarflexion and 0.40 Nm/deg (22.92 Nm/rad) for 0–20 deg in dorsiflexion. Similar to the hip joint, the stiffness of the robot is even closer to linear, but is stiffer than a human. The stiffness at 20 psi (the closest to that of a human) is 1.3 Nm/deg (74.49 Nm/rad) for plantarflexion and 2.4 Nm/deg (137.51 Nm/rad) for dorsiflexion.

While there is an asymmetry in the restorative force supplied in the sagittal plane of motion, there is not one in the transverse plane of motion because the ROM for ankle inversion and eversion are relatively close, unlike the dorsiflexion and plantarflexion DOF. Figure 17 shows the torque required to rotate the ankle joint during five nonconsecutive trials for the ankle (*a*) inversion and (*b*) eversion. This DOF has similar force profiles, which was expected since the joint is symmetrical in this direction. We were unable to find any reliable human data to compare the results of eversion and inversion.

4 Discussion

This article demonstrates several types of novel joint designs almost all of which utilize a hybrid design that incorporates both rigid and compliant components. While the knee joint is not in this hybrid style, the design uses contact surfaces instead of a floating linkage or rolling knee design, locks in the upright position, and has a changing center of rotation [39]. These designs are shown to have beneficial properties that are like their human counterpart and enable the creation of a robotic platform with human-like kinematics and abilities such as range of motion (ROM), a locking knee, and dynamic joint stiffness. Using a platform similar to the one described here, researchers will be able to more accurately test models of human locomotion and balance control [52], by implementing them directly on a robotic platform with similar kinematics and dynamics. This work demonstrates that the development of such robotic models is feasible, even if some of the dynamic results are not yet ideal.

4.1 Comparison With Human Joints. Specifically, the synovial inspired joints offer a useful way to bridge the gap between completely soft robots and the traditional rigid robot designs that are typically used for bipedal testing [16,53]. These joints use a cushion of air to aid in impact resistance. They also add damping to the system to reduce the wear from the cyclical loads incurred during walking. As the angle of flexion or extension increases, the restoring force generated by the joint increases. This is similar behavior to how joints of humans and other mammals work [45,46]. Furthermore, the stiffness of the joint can be controlled by controlling the pressure in the joint. Studies of human movement also seem to indicate that joint stiffness is controlled dynamically [34,54]. Both these properties have the potential to increase the controllability of joints when compared to a traditional ball and socket type joint through a naturally stable architecture.

Unfortunately, it is hard to directly compare our properties with humans as there are only a few studies that look at the passive dynamics of human synovial joints [55,56]. In their work, researchers use cadaver joints to test mechanical properties of the joint capsule itself, which is useful in understanding the mechanical properties of the joints, but not how the joint responds dynamically [54]. Furthermore, there are challenges with measuring joint capsule dynamics using cadaver joints because these joints are removed from their normal pathology, which can eliminate other interactions that occur in vivo [34]. We have also found several studies that use living subjects to test joint stiffness [45,46,57]. Both types of studies show that as the angle of deflection increases, the joint produces a restoring force that increases exponentially,

while the restoring force of the robot joint increases in a linear manner. By using the models created from human data, our data can be compared with a human model [51]. Because no model for hip adduction or abduction could be located, our measured values are compared using the model created for hip extension and flexion. Figure 15 shows the values of the hybrid hip joint in (*a*) abduction and (*b*) adduction plotted with a zero-shifted model of human hip extension and flexion.

As shown in Figs. 15 and 16, the created hybrid joint is stiffer than the human counterpart (a smaller angle change is achieved with the same applied torque). In addition, the restoring forces for a human joint have two components. Near the joint, the stiffness seems relatively linear. However, at some point, it transitions from linear to an almost exponential rate. The hybrid joint only increases in a linear fashion, creating a closer fit at larger ranges of motion; however, joints that utilize a less stiff braided pneumatic actuator for attachment will likely have a better overall fit to the human data. Future work should be done to determine the relationship between stiffness on the robot's locomotion and balancing performance to determine if a less stiff joint improves or hinders control.

In addition to being a function of angle, human joint stiffness is also a function of muscle activation and other joint angles. This further complicates the picture, making it difficult to determine experimentally joint stiffness during different tasks such as walking, running, and squatting. As the stiffness of our joint could be modified in real time by changing the internal pressure, our design could provide an effective mechanism to test the effect that different joint stiffness has on the dynamics and control of the system. Direct comparisons with human kinematic, kinetic, and muscle activation data (which is easier to collect than internal joint stiffness data) can then be made to make an estimate on the internal stiffness of the human body. Further human cadaver and in vivo testing should be done to determine the restorative force of human synovial joints to enable an accurate comparison with our data.

Active control strategies could also be employed to better match the human synovial joint stiffness and alter gait dynamics. Because the feet are a highly coupled system and the design provides for real-time adjustment of internal pressure, this could further improve energy efficiency and balance. For example, toe stiffness has been shown to have, in some cases, a larger impact in gait dynamics than adjusting ankle stiffness [58]. Active control has also been shown to improve disturbance rejection in humanoid systems [59]. Future work should be done to determine efficient control strategies for this type of system.

In addition to active control strategies in the joints themselves, joint stiffness could be regulated by the artificial muscles themselves, as is done with most biological systems. Changes in muscle stiffness and co-contraction should increase joint stiffness by causing increased compression of the BPA joints.

Future work should also look at the development of BPAs designed specifically for synovial joints. Different materials could be utilized to more closely match the human data. In addition, different weave designs and materials will be necessary to capture three degrees-of-freedom about the hip joint. Our model was not able to effectively achieve hip flexion and extension movements, a very critical movement of locomotion and other behaviors.

While computing the inertia and other properties of the constructed parts is outside the scope of our current paper, we plan to address this with future work. Finally, cyclic load testing also needs to be performed to determine the average lifetime of the joints and to characterize any changes in behavior as they reach the end of their life cycle.

4.2 Use in Robotics and Prosthetics. Our work suggests that MRI/CT modeling of joints can provide enough biomechanical information that result in accurately modeled in vivo joints. We have demonstrated that medical scans can be used to create a mechanical equivalent for the purposes of robotics and prosthetics research and development. This framework gives researchers the ability to recreate models of joints from living subjects and in loading conditions that may be difficult or impossible to achieve with cadaver joints.

These joints offer several potential advantages over traditional robotic joints. For example, the use of the BPA at the ankle and toe joints will provide damping at the ankle during heel strike, which may reduce joint wear and improve controllability while also providing energy capture during the loading phase preceding toe off. By using BPAs to approximate, the articular capsule of the synovial joint also reduces the effects of catastrophic failure. If the bladder of the BPA is punctured, the fiber braiding that limits the bladder deformation will not allow joint dislocation, and still limits ROM of the joint. The designed knee joint has a locking mechanism like the human knee, which saves energy. The changing center of rotation gives the joint a compact size but increases the moment arm of the extensor muscle during flexion. By using contacting surfaces to distribute, the load should substantially increase the life of the joint by spreading the force across larger, and more fatigue resistant areas than are in a typical hinge joint or motor.

Several of the designed synovial joints are also connected using internal tubing. Therefore, loading one joint will change the pressure of the other connected joints. While this adds to the complexity of the dynamic response of the test-bed, there are several benefits that the linking provides. For instance, when walking during the toe off phase of the gait cycle, the load on the lateral and medial toe of the foot compress the air in the toes increasing the pressure in the ankle. This increase in pressure helps to keep the ankle in line with the tibia, which creates a more secure connection between the two contacting surfaces of the joint. This is illustrated by the reduction in the ROM of the joint as the pressure increases.

Some of the designed synovial joints tested had a maximum ROM lower than the average adult male. Future work includes redesigning the extension/flexion degree-of-freedom of the hip to match better the ROM of the human hip. Future work will also be needed to determine the relationship between BPA sleeve length, the initial gap between loading surfaces, the surface geometry, and the ROM the joint can achieve. Better understanding of these parameters will guide further joint designs and will give the ability to predict joint ROM prior to physical testing.

Recent advances in technology and manufacturing have opened up a new door in bio-mimetic robotics. These advances enable us to more accurately capture and recreate the bone and joint structures that are seen in animals. More design and experimental work is needed for us to fully realize this potential and build realistic animal inspired robots, such as robots based on dogs or other quadrupeds. The work presented here demonstrates a design approach that utilizes new manufacturing technologies to capture several kinematic and passive dynamic aspects of human skeletons that has not been realized earlier. Further research in this area will continue to move this design approach further, enabling the building of highly dynamic and realistic human and animal robot models in the future.

5 Conclusions

This article presents several types of joints employing MRI and CT scans to inform the design process. These joints have several desirable properties for robotic and prosthetic applications, such as a hybrid soft-rigid construction, real-time adjustable joint stiffness and damping, large contact surfaces for improved joint life, energy saving mechanisms such as "screw home" analog found in the human knee, and energy storing during the pre-swing phase of gait. We then validate our design methodology by testing the range of motion and joint stiffness through several different joint pressures. In the future, this test-bed will be used to develop different active and passive stiffness control strategies.

Acknowledgment

The authors acknowledge the support of the Mechanical and Materials Engineering Department in the Maseeh College of Engineering at Portland State University and the support of the UK Engineering and Physical Sciences Research Council (EPSRC) under grant reference EP/P022588/1.

Conflict of Interest

There are no conflicts of interest.

Data Availability Statement

The authors attest that all data for this study are included in the paper.

Nomenclature

T = torque
F = force
L = distance from the applied force to the centroid.
θ = change in the angle of the joint.

References

[1] Steele, A., Hunt, A., and Etoundi, A., 2018, "Biomimetic Knee Design to Improve Joint Torque and Life for Bipedal Robotics," *Towards Autonomous Robotic Systems. TAROS 2018. Lecture Notes in Computer Science*, M. Giuliani, T. Assaf, and M. Giannaccini, eds., vol. 10965. Springer, Cham.
[2] Tytell, E., Holmes, P., and Cohen, A. H., 2011, "Spikes Alone Do Not Behavior Make: Why Neuroscience Needs Biomechanics," Curr. Opin. Neurobiol., **21**(5), pp. 816–822.
[3] Ijspeert, A. J., 2014, "Biorobotics: Using Robots to Emulate and Investigate Agile Locomotion," Science, **346**(6206), pp. 196–203.
[4] Iida, F., and Ijspeert, A. J., 2016, "Biologically Inspired Robotics," Siciliano, B. Khatib, O., eds., *Springer Handbook of Robotics*, Springer International Publishing, Gewerbestrasse, Switzerland, pp. 2015–2034.
[5] Asano, Y., Kozuki, T., Ookubo, S., Kawamura, M., Nakashima, S., Katayama, T., Yanokura, I., Hirose, T., Kawaharazuka, K., Makino, S., Kakiuchi, Y., Okada, K., and Inaba, M., 2016, "Human Mimetic Musculoskeletal Humanoid Kengoro Toward Real World Physically Interactive Actions," 2016 IEEE-RAS 16th International Conference on Humanoid Robots (Humanoids), Coral Beach, Cancun, Mexico, Nov. 15–17, pp. 876–883.
[6] Kojima, K., Karasawa, T., Kozuki, T., Kuroiwa, E., Yukizaki, S., Iwaishi, S., Ishikawa, T., Koyama, R., Noda, S., Sugai, F., Nozawa, S., Kakiuchi, Y., Okada, K., and Inaba, M., 2015, "Development of Life-Sized High-Power Humanoid Robot JAXON for Real-World Use," 2015 IEEE-RAS 15th International Conference on Humanoid Robots (Humanoids), Seoul, South Korea, Nov. 3–5, pp. 838–843.
[7] Shin, H., Ikemoto, S., and Hosoda, K., 2018, "Constructive Understanding and Reproduction of Functions of Gluteus Medius by Using a Musculoskeletal Walking Robot," Adv. Rob., **32**(4), pp. 202–214.
[8] Asano, Y., Mizoguchi, H., Kozuki, T., Motegi, Y., Urata, J., Nakanishi, Y., Okada, K., and Inaba, M., 2013, "Achievement of Twist Squat by Musculoskeletal Humanoid With Screw-Home Mechanism," IEEE/RSJ International Conference on Intelligent Robots and Systems, Tokyo, Japan, Nov. 3–7, pp. 4649–4654.
[9] Magdalena, N,-W, Artur, W, 2018, "The Machining Process and Multi-sensor Measurements of the Friction Components of Total Hip Joint Prosthesis," Measurement, **116**(1), pp. 56–67.
[10] Mohanty, R. K., Mohanty, R. C., and Sabut, S. K., 2020, "A Systematic Review on Design Technology and Application of Polycentric Prosthetic Knee in Amputee Rehabilitation," Phys. Eng. Sci. Med., **43**(3), pp. 1–18.
[11] Kapur, T., Pieper, S., Fedorov, A., Fillion-Robin, J.-C., Halle, M., O'Donnell, L., Lasso, A., Ungi, T., Pinter, C., Finet, J., Pujol, S., Jagadeesan, J., Tokuda, J., Norton, I., San Jose Estepar, R., Gering, D., Aerts, H., Jakab, M., Hata, N., Ibanez, L., Blezek, D., Miller, J., Aylward, S., Grimson, E., Fichtinger, G., Wells, W., Lorensen, W., Schroeder, W., and Kikinis, R., 2016, "Increasing the Impact of Medical Image Computing Using Community-Based Open-Access Hackathons: The NA-MIC and 3D Slicer Experience," Med. Image Anal., **33**(1), pp. 176–180.
[12] Swogger, S. E., 2018, "The Interactive Web–3d Printing Resources for Medical Academic Libraries," J. Electronic Res. Med. Librar., **15**(3–4), pp. 144–148.
[13] Bücking, T. M., Hill, E. R., Robertson, J. L., Maneas, E., Plumb, A. A., and Nikitichev, D. I., 2017, "From Medical Imaging Data to 3D Printed Anatomical Models," PLoS. One., **12**(5), p. e0178540.
[14] Schmidt, R., and Singh, K., 2010, "Meshmixer: An Interface for Rapid Mesh Composition," Special Interest Group on Computer Graphics and Interactive Techniques Conference, Los Angeles, CA, July 26–30.
[15] Alderink, G. J., 1991, "The Sacroiliac Joint: Review of Anatomy, Mechanics, and Function," J. Ortho. Sports Phys. Therapy, **13**(2), pp. 71–84.
[16] Alghooneh, M., Wu, C. Q., and Esfandiari, M., 2016, "A Passive-Based Physical Bipedal Robot With a Dynamic and Energy-Efficient Gait on the Flat Ground," IEEE/ASME Trans. Mechat., **21**(4), pp. 1977–1984.
[17] Steele, A. G., and Hunt, A. J., 2018, "Braided Pneumatic Actuators as a Variable Stiffness Approximation of Synovial Joints," Conference on Biomimetic and Biohybrid Systems, Paris, France, July 17–20, Springer, pp. 450–458.
[18] Harty, M, 1984, "The Anatomy of the Hip Joint," *Surgery of the Hip Joint*, R. G. Tronzo, ed., Springer, New York, pp. 45–74.
[19] Jamali, A. A., Mak, W., Wang, P., Tai, L., Meehan, J. P., and Lamba, R., 2013, "What Is Normal Femoral Head/Neck Anatomy? An Analysis of Radial CT Reconstructions in Adolescents," Clin. Orthop. Relat. Res., **471**(11), pp. 3581–3587.
[20] Soucie, J. M., Wang, C., Forsyth, A., Funk, S., Denny, M., Roach, K. E., and Boone, D., 2011, "Range of Motion Measurements—Reference Values and a Database for Comparison Studies," Haemophilia, **17**(3), pp. 500–507.
[21] Kouyoumdjian, P., Coulomb, R., Sanchez, T., and Asencio, G., 2012, "Clinical Evaluation of Hip Joint Rotation Range of Motion in Adults," Orthop. Traumatol.: Surgery Res., **98**(1), pp. 17–23.
[22] Edwards, W. T., 2007, "Effect of Joint Stiffness on Standing Stability," Gait Post., **25**(3), pp. 432–439.
[23] Azaman, A., and Yamamoto, S.-i., 2014, "Balance Process During Repeated Surface Perturbation: Adaptation Response of Joint Stiffness and Muscle Activation," 2014 IEEE Conference on Biomedical Engineering and Sciences (IECBES), Miri, Malaysia, Dec. 8–10, IEEE, pp. 291–294.
[24] Wu, H.-H., Wang, D., Ma, A.-B., and Gu, D.-Y., 2016, "Hip Joint Geometry Effects on Cartilage Contact Stresses During a Gait Cycle," Conference Proceedings: Annual International Conference of the IEEE Engineering in Medicine and Biology Society, Orlando, FL, Aug. 16–20, pp. 6038–6041.
[25] Kazemi, S. M., Qoreishy, M., Keipourfard, A., Sajjadi, M. M., and Shokraneh, S., 2016, "Effects of Hip Geometry on Fracture Patterns of Proximal Femur," Arch, Bone Joint Surgery, **4**(3), pp. 248–252.
[26] Horton, M. G., and Hall, T. L., 1989, "Quadriceps Femoris Muscle Angle: Normal Values and Relationships With Gender and Selected Skeletal Measures," Phys. Therapy, **69**(11), pp. 897–901.
[27] Sanchez, H. M., de Morais Sanchez, E. G., Baraúna, M. A., and de Tavares Cant, R. S., 2014, "Evaluation of Q Angle in Differents Static Postures," Acta Ortop. Bras, **22**(6), pp. 325–329.
[28] Emami, M.-J., Ghahramani, M.-H., Abdinejad, F., and Namazi, H., 2007, "Q-angle: An Invaluable Parameter for Evaluation of Anterior Knee Pain," Arch. Iranian Med., **10**(1), pp. 24–26.
[29] Fajar, J. K., Taufan, T., Syarif, M., and Azharuddin, A., 2018, "Hip Geometry and Femoral Neck Fractures: A Meta-Analysis," J. Orthop. Trans., **13**(1), pp. 1–6.
[30] Hartel, M. J., Petersik, A., Schmidt, A., Kendoff, D., Nüchtern, J., Rueger, J. M., Lehmann, W., and Grossterlinden, L. G., 2016, "Determination of Femoral Neck Angle and Torsion Angle Utilizing a Novel Three-Dimensional Modeling and Analytical Technology Based on CT Datasets," PLoS. One., **11**(3), p. e0149480.
[31] Madeti, B. K., Chalamalasetti, S. R., and Bolla Pragada, S. K. S. s. r., 2015, "Biomechanics of Knee Joint—A Review," Front. Mech. Eng., **10**(2), pp. 176–186.
[32] Abulhasan, J. F., and Grey, M. J., 2017, "Anatomy and Physiology of Knee Stability," J. Funct. Morph. Kinesiol., **2**(34), p. 061010.
[33] Proffen, B. L., McElfresh, M., Fleming, B. C., and Murray, M. M., 2012, "A Comparative Anatomical Study of the Human Knee and Six Animal Species," Knee, **19**(4), pp. 493–499.
[34] Proffen, B. L., McElfresh, M., Fleming, B. C., and Murray, M. M., 2012, "Reconstructing the Knee Joint Mechanism From Kinematic Data," Math. Comput. Model. Dyn. Syst., **16**(5), pp. 403–415.
[35] Anglin, C., Ho, K. C., Briard, J.-L., de Lambilly, C., Plaskos, C., Nodwell, E., and Stindel, E., 2008, "In Vivo Patellar Kinematics During Total Knee Arthroplasty," Comput. Aided Surgery, **13**(6), pp. 377–391.
[36] Ozada, N., 2016, "Biomechanical Model of Knee Collateral Ligament Injury With Six Degrees of Freedom," Med. Biolog. Eng. Comput., **54**(5), pp. 821–830.
[37] Lamberto, G., Richard, V., Dumas, R., and Valentini, P. P., 2016, "Modeling the Human Tibiofemoral Joint Using Ex Vivo Determined Compliance Matrices," ASME J. Biomech. Eng., **138**(6), p. 061010.
[38] Burgess, S., and Etoundi, A., 2014, "Performance Maps for a Bio-Inspired Robotic Condylar Hinge Joint," ASME J. Mech. Des., **136**(11), p. 115002.
[39] Steele, A. G., Hunt, A., and Etoundi, A. C., 2017, "Development of a Bio-Inspired Knee Joint Mechanism for a Bipedal Robot," *Biomimetic and Biohybrid Systems* (Lecture Notes in Computer Science), M. Mangan, M. Cutkosky, A. Mura, P. F. M. J. Verschure, T. Prescott, and N. Lepora, eds., Springer, Cham, pp. 418–427.
[40] Brockett, C. L., and Chapman, G. J., 2016, "Biomechanics of the Ankle," Orthop. Trauma, **30**(3), pp. 232–238.
[41] Milner, C. E., and Soames, R. W., 1998, "Anatomy of the Collateral Ligaments of the Human Ankle Joint," Foot Ankle Inter, **19**(11), pp. 757–760.
[42] Kelikian, A. S., and Sarrafian, S. K., 2011, *Sarrafian's Anatomy of the Foot and Ankle: Descriptive, Topographic, Functional*, Lippincott Williams & Wilkins, Philadelphia, PA, Google-Books-ID: I8h6bDR0SLMC.
[43] Gwani, A. S., Asari, M. A., and Mohd Ismail, Z. I., 2017, "How the Three Arches of the Foot Intercorrelate," Folia Morphol., **76**(4), pp. 682–688.
[44] Hashimoto, K., Takezaki, Y., Hattori, K., Kondo, H., Takashima, T., Lim, H.-o., and Takanishi, A., 2010, "A Study of Function of Foot's Medial Longitudinal Arch Using Biped Humanoid Robot," 2010 IEEE/RSJ International Conference on Intelligent Robots and Systems, Taipei, Taiwan, Oct. 18–22, pp. 2206–2211.

[45] Amiri, P., and Kearney, R. E., 2017, "Ankle Intrinsic Stiffness is Modulated by Postural Sway," 2017 39th Annual International Conference of the IEEE Engineering in Medicine and Biology Society (EMBC), Jeju, South Korea, July 11–15, IEEE, pp. 70–73.
[46] Misgeld, B. J. E., Zhang, T., Lüken, M. J., and Leonhardt, S., 2017, "Model-Based Estimation of Ankle Joint Stiffness," Sensors, **17**(4), p. 713.
[47] González-Estrada, O. A., Pertuz, A., and Quiroga Mendez, J. E., 2018, "Evaluation of Tensile Properties and Damage of Continuous Fibre Reinforced 3d-Printed Parts," Key Engineering Materials, **774**, pp. 161–166.
[48] Dickson, A. N., Barry, J. N., McDonnell, K. A., and Dowling, D. P., 2017, "Fabrication of Continuous Carbon, Glass and Kevlar Fibre Reinforced Polymer Composites Using Additive Manufacturing," Addit. Manuf., **16**(1), pp. 146–152.
[49] Hetrick, D. R., Sanei, S. H. R., Bakis, C. E., and Ashour, O., 2021, "Evaluating the Effect of Variable Fiber Content on Mechanical Properties of Additively Manufactured Continuous Carbon Fiber Composites," J. Reinf. Plast. Compos., **40**(9–10), pp. 365–377.
[50] Chen, J.-w., Dai, J., Yang, J.-h., Huang, T., Zhang, N., and Wang, Y., 2013, "Annealing-Induced Crystalline Structure and Mechanical Property Changes of Polypropylene Random Copolymer," J. Mater. Res., **28**(22), pp. 3100–3108.
[51] Riener, R., and Edrich, T., 1999, "Identification of Passive Elastic Joint Moments in the Lower Extremities," J. Biomech., **32**(5), pp. 539–544.
[52] Hilts, W. W., Szczecinski, N. S., Quinn, R. D., and Hunt, A. J., 2019, "A Dynamic Neural Network Designed Using Analytical Methods Produces Dynamic Control Properties Similar to An Analogous Classical Controller," IEEE Control Syst. Lett., **3**(2), pp. 320–325.
[53] Kim, B.-H., 2013, "Work Analysis of Compliant Leg Mechanisms for Bipedal Walking Robots," Inter. J. Adv. Rob. Syst., **10**(9), p. 334.
[54] Itoi, F., Grabowski, J. J., Morrey, B. F., and An, K.-N., 1993, "Capsular Properties of the Shoulder," Tohoku J. Experi. Med., **171**(3), pp. 203–210.
[55] Vaz, J. A., and Hirai, S., 2004, "A Simplified Model for a Biomechanical Joint With Soft Cartilage," 2004 IEEE International Conference on Systems, Man and Cybernetics (IEEE Cat. No.04CH37583), The Hague, Netherlands, Oct. 10–13, Vol. 1, pp. 756–761.
[56] Macirowski, T., Tepic, S., and Mann, R. W., 1994, "Cartilage Stresses in the Human Hip Joint," ASME J. Biomech. Eng., **116**(1), pp. 10–18.
[57] Heger, H., Wank, V., and Blickhan, R., 2012, "A Quasi-Linear Viscoelastic Model for the Passive Properties of the Human Hip Joint," J. Mech. Med. Biol., **12**(1), p. 1250015.
[58] Honert, E. C., Bastas, G., and Zelik, K. E., 2018, "Effect of Toe Joint Stiffness and Toe Shape on Walking Biomechanics," Bioinspi. Biomim., **13**(6), p. 066007.
[59] Spyrakos-Papastavridis, E., Kashiri, N., Childs, P. R., and Tsagarakis, N. G., 2018, "Online Impedance Regulation Techniques for Compliant Humanoid Balancing," Rob. Auton. Syst., **104**(1), pp. 85–98.